Efficient 3-D Capacitance Extraction Considering Lossy Substrate With Multilayered Green's Function

Zuochang Ye, *Student Member, IEEE*, Wenjian Yu, *Member, IEEE*, and Zhiping Yu, *Senior Member, IEEE*

***Abstract*—An efficient algorithm for extraction of three-dimensional (3-D) capacitance on multilayered and lossy substrates is presented. The new algorithm presents a major improvement over the quasi-3-D approach used in a Green's function-based solver and takes into consideration the sidewalls of 3-D conductors. To improve the efficiency of the computation and the transformation of the Green's function, a nonuniform grid is adopted. The most computationally intensive part in the transformation of the Green's function is computed separately as technology-independent matrices T_k foremost. Once computed, T_k can be stored and used for any technology, thus the storage requirement and computational complexity are reduced from $\mathcal{O}(S^2)$ and $\mathcal{O}(S^2 \log S^2)$, respectively, to just $\mathcal{O}[(\log S_{\max})^2]$. Extensive tests have been performed to verify the new algorithm, and its accuracy has been established by comparing with other programs.**

***Index Terms*—Capacitance extraction, Green's function, nonuniform grid, substrate coupling.**

I. Introduction

IT BECOMES more critical that three-dimensional (3-D) effects should be considered accurately in modeling capacitance on radio-frequency (RF) CMOS integrated circuits (ICs) because of shrunken feature size and increased operation frequency. The boundary element method (BEM) is an efficient method for this problem, since only conductor surfaces and interfaces between different material regions need to be discretized, and thus the computational expense is greatly reduced, compared with finite-difference or finite-element schemes, e.g., Raphael [1] and HFSS [2].

Great efforts have been made in the BEM-based 3-D capacitance extraction, such as the fast multi-pole method (FMM) [3], the singular value decomposition (SVD) method [4], the hierarchical method [5], and the quasi-multiple medium (QMM) method [6]. Other methods, not confined to BEM, such as sparse matrix canonical grid (SMCG) [7] and adaptive integral method (AIM) [8] are also presented. All of these methods, however, focus mainly on the fast solving of the resulted linear system, i.e., the so-called $\mathbf{Pq} = \mathbf{v}$ problem.

In this paper, we study the efficient computation of potential coefficient matrix $\mathbf{P}$ for multilayered and lossy substrate based on Green's function [9], [10]. In this method, the Green's function is calculated and stored based on the process technology only, thus the dielectric interfaces do not need to be discretized. As a result, the size of the linear system is greatly reduced. Furthermore, the algorithm in this paper can be combined with some of the aforementioned numerical methods to improve the efficiency.

In [9], the chip structure is assumed to be confined by rectangle electric and magnetic walls. Considering the Neumann boundary condition at the magnetic walls, the Green's function can be expanded in cosine series, and thus the fast Fourier transform (FFT) can be applied to accelerate the summation of cosine series. By introducing the concept of complex permittivity [11], this method can handle lossy substrate with little extra effort. The original algorithm was implemented in software ASITIC [12].

However, in ASITIC, only analytical integration over horizontal panels is conducted, such that the conductors are treated as two-dimensional (2-D) sheets, preventing its use in 3-D capacitance extraction. Mathematically, the Green's function in [10] can be integrated analytically in the z-direction, thus the sidewall capacitance can be computed. In practice, however, there are some difficulties, because, to preserve the numerical stability, the Green's function in the z-direction is obtained through a complicated recursive procedure [10]. The resulted expression is a continual multiplication, which cannot be integrated analytically. Although measures have been taken in [13] by considering both the bottom and the top plates of conductors, the sidewall capacitance still cannot be handled accurately. In [14], conductors are cut horizontally into slices in order to include 3-D effects, but this amounts to volume discretization, leading to an enormous increase in variable number.

Another major disadvantage arises from the FFT-accelerated discrete cosine transform (DCT). Although it dramatically reduces the computational cost for the doubly infinite series, it requires meshing of the whole chip uniformly, since the mesh size is related to the ratio of the chip dimension to the minimum panel size. With the feature size shrunk to the deep-submicrometer regime while the chip size stays on the order of millimeters, this uniform meshing results in an unacceptable amount of memory and time to perform the transformation and store the transformed matrix.

In this paper, we derived a new formula for the recursive computation of Green's function, which can be integrated stably over the sidewalls of the conductor to accomplish true 3-D extraction. The efficiency for computing and storing the Green's function is also improved by using a nonuniform grid.

In Section II, the Green's function approach for capacitance extraction is reviewed, and the derivation of the recursive computation of Green's function is redone in a simpler and more

Manuscript received September 3, 2005; revised December 21, 2006. This work was supported by the Ministry of Science and Technology in China under Research Grant 2004AA1Z11050 of the National 863 Plan. The work of W. Yu was supported by the NSFC under Grant 60401010.

Z. Ye and Z. Yu are with the Computer-Aided Design Group, Institute of Microelectronics, Tsinghua University, Beijing 100084, China (e-mail: yzc02@mails.tsinghua.edu.cn; yuzhip@tsinghua.edu.cn).

W. Yu is with the EDA Laboratory, Department of Computer Science and Technology, Tsinghua University, Beijing 100084, China (e-mail: yu-wj@tsinghua.edu.cn).

Digital Object Identifier 10.1109/TMTT.2006.873630

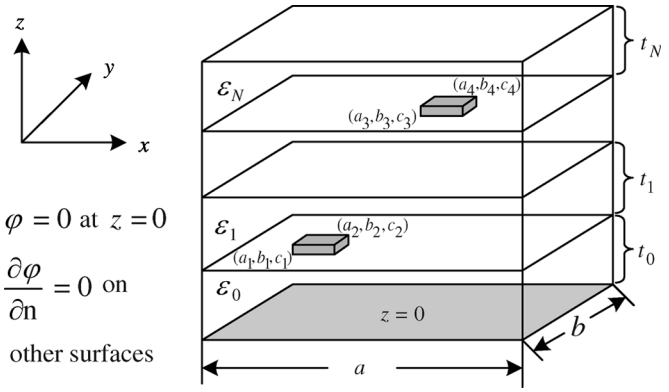

Fig. 1. Geometry and boundary condition of the multilayer substrate.

stable form. In Section III, the Green's function in the z-direction is rederived, and the numerical stability is studied. In Section IV, the surfaces of conductors are classified to four types, and analytical integral of the coefficients of potential for each type is derived. In Section V, an efficient method for computing the Green's function is presented. Experiment results are shown in Section VI, and conclusions are given in Section VII.

II. Background

The substrate is characterized in [9] as a multilayered structure, as shown in Fig. 1. Each layer has a thickness and a uniform permittivity and conductivity. Conductors are embedded in the layers. The objective of the parasitics extraction is to compute the capacitance matrix $\mathbf{C}$ for a multiconductor geometry.

To determine the jth column of $\mathbf{C}$, we need only to solve for the surface charges on each conductor produced by raising conductor j to unit potential while grounding the rest of the conductors. Then, C_{ij} is numerically equal to the charge q_i on conductor i. The charge q_i is obtained by solving the linear system

$$\mathbf{Pq} = \mathbf{v} \tag{1}$$

where $\mathbf{q}$ is the vector of panel charges, $\mathbf{v}$ is the vector of panel potentials which are supposedly known, and $\mathbf{P}$ is the potential coefficient matrix. Each entry of $\mathbf{P}$, i.e., p_{ij}, is the average potential v_i over panel i due to the unit charge uniformly distributed on panel j. Using the Galerkin method and assuming a piece-wise constant charge distribution, p_{ij} can be computed by convolving the charge distribution with the Green's function as

$$p_{ij} = \frac{q_j}{A_i A_j} \int_{\mathbf{r}\in A_i} \int_{\mathbf{r}'\in A_j} G(\mathbf{r},\mathbf{r}')d\mathbf{r}d\mathbf{r}'. \tag{2}$$

The Green's function $G(\mathbf{r}',\mathbf{r})$ can be computed by solving the Poisson's equation

$$\nabla^2 G(\mathbf{r},\mathbf{r}') = \frac{-\delta_m(\mathbf{r}-\mathbf{r}')}{\dot{\varepsilon}} \tag{3}$$

where

$$\dot{\varepsilon} = \varepsilon + \frac{\sigma}{j\omega} \tag{4}$$

is the complex medium permittivity [11]. By the use of $\dot{\varepsilon}$ instead of ε, both ohmic and displacement currents are accounted for, and thus the frequency-dependent effects for conductive substrate are included.

The use of the Green's function greatly simplifies the problem by implicitly taking into account the boundary conditions, making it unnecessary to discretize the boundaries. In this case, only the actual conductors require discretization. The Green's function has been previously computed in analytical form and shown to be [9]

$$G(x,y,z,x',y',z') = \sum_{m=0}^{\infty}\sum_{n=0}^{\infty} f_{mn}(z,z')\cos(\delta_m x')\cos(\xi_n y') \times \cos(\delta_m x)\cos(\xi_n y) \tag{5}$$

where $\delta_m = m\pi/a$ and $\xi_n = n\pi/b, a, b$ are the lateral dimensions of the substrate in the x- and y-directions, respectively. f_{mn} is obtained by solving the Poisson's equation in the z-direction along with the boundary conditions in this dimension, and it is shown in [9] that

$$f_{mn}(z,z') = \frac{C_{mn}\cosh(\gamma_{mn}z')\cosh(\gamma_{mn}z)}{ab\dot{\epsilon}_s\gamma_{mn}\left(\Gamma_k^u\beta_k^l - \Gamma_k^l\beta_k^u\right)} \times \left[\beta_k^{u,l}\tanh(\gamma_{mn}z') - \Gamma_k^{u,l}\right] \times \left[\beta_k^{u,l}\tanh(\gamma_{mn}z') - \Gamma_k^{u,l}\right] \tag{6}$$

where $\gamma_{mn} = \sqrt{(m\pi/a)^2 + (n\pi/b)^2}$, and $\dot{\epsilon}_s$ is the complex permittivity of the source layer. The subscript "k" is the index for each layer. The superscripts "u" and "l" are for upper and lower cases, respectively.

Direct computation of (6) is numerically instable. To overcome this, [10] presents a numerical stable algorithm, and [15] further improves the stability. In both methods, following [9], f_{mn} is derived using hyperbolic functions as in (6). Accordingly, to solve the numerical stability, the resulting formulas, i.e., [10, eqs. (51a), (51b)], behave as continuing multiplications, for which there exists no closed-form integration in the z-direction, and the capacitance regarding sidewalls can not be computed. Such that (6) should be rederived, and the numerical stability issue should be addressed.

III. Robust Computation of Green's Function Using Exponential Functions

To rederive the formula for Green's function in the z-direction, we start from [10, eq. (14)], shown as

$$\frac{ab}{4}\left(\frac{\mathrm{d}^2 Z}{\mathrm{d}z^2} - \gamma_{mn}^2 Z\right) = -\frac{\delta_m(z-z')}{\epsilon_k} \tag{7}$$

where $Z = f_{mn}/\cos(\delta_m x)\cos(\xi_n y)$. Z should satisfy the following boundary conditions at the source point, the interfaces of adjacent layers, and the top and bottom of the whole structure, respectively:

$$Z_k^l(z') = Z_k^u(z') \tag{8}$$

$$\left.\frac{\mathrm{d}Z_k}{\mathrm{d}z}\right|_{z'-\delta_m}^{z'+\delta_m} = -\frac{C_{mn}}{ab\epsilon_k} \tag{9}$$

$$Z_k|_{z=z_k} = Z_{k-1}|_{z=z_k} \tag{10}$$

$$\epsilon_k \left.\frac{\mathrm{d}Z_k}{\mathrm{d}z}\right|_{z=z_k} = \epsilon_{k-1} \left.\frac{\mathrm{d}Z_{k-1}}{\mathrm{d}z}\right|_{z=z_k} \tag{11}$$

$$Z_0|_{z=0} = 0 \tag{12}$$

$$\left.\frac{\mathrm{d}Z_N}{\mathrm{d}z}\right|_{z=z_{N+1}} = 0. \tag{13}$$

The most general solution for (7), considering the boundary conditions (8) and (9) at point z', is

$$\begin{aligned} f_{mn}(z',z) &= \frac{C_{mn}}{ab\dot{\varepsilon}_s\gamma_{mn}} \\ &\quad\times\frac{\left(\alpha_s^{u,l}e^{\gamma_{mn}z'}+\beta_s^{u,l}e^{-\gamma_{mn}z'}\right)\left(\alpha_f^{l,u}e^{\gamma_{mn}z}+\beta_f^{l,u}e^{-\gamma_{mn}z}\right)}{\alpha_s^u\beta_s^l-\alpha_s^l\beta_s^u} \\ &= \left(\alpha_s e^{\gamma_{mn}z'}+\beta_s e^{-\gamma_{mn}z'}\right)\left(\alpha_f e^{\gamma_{mn}z}+\beta_f e^{-\gamma_{mn}z}\right) \end{aligned} \tag{14}$$

where the subscript s denotes the source layer, and the subscript f denotes the field layer. The above formula and (6) are equal mathematically, while they are different numerically from each other, especially when the stability problem is involved.

The boundary conditions on the interface of each adjacent layer, i.e., (10) and (11), lead to recursive relations that the coefficients must satisfy as follows:

$$\begin{pmatrix}\alpha_k^l\\ \beta_k^l\end{pmatrix} = \mathbf{A_k}\begin{pmatrix}\alpha_{k-1}^l\\ \beta_{k-1}^l\end{pmatrix} \tag{15}$$

$$\begin{pmatrix}\alpha_k^u\\ \beta_k^u\end{pmatrix} = \mathbf{A_{k+1}^{-1}}\begin{pmatrix}\alpha_{k+1}^u\\ \beta_{k+1}^u\end{pmatrix} \tag{16}$$

respectively for the cases that the field point is above and below the source point. In the above two equations, the matrices $\mathbf{A_k}$ and $\mathbf{A_k^{-1}}$ are defined as

$$\mathbf{A_k} = \frac{1}{2}\begin{bmatrix}(1+p_k)e^{\gamma_{mn}t_{k-1}} & (1-p_k)e^{-\gamma_{mn}t_{k-1}}\\ (1-p_k)e^{\gamma_{mn}t_{k-1}} & (1+p_k)e^{-\gamma_{mn}t_{k-1}}\end{bmatrix} \tag{17}$$

$$\mathbf{A_k^{-1}} = \frac{1}{2p_k}\begin{bmatrix}(1+p_k)e^{-\gamma_{mn}t_{k-1}} & (p_k-1)e^{-\gamma_{mn}t_{k-1}}\\ (p_k-1)e^{\gamma_{mn}t_{k-1}} & (1+p_k)e^{\gamma_{mn}t_{k-1}}\end{bmatrix} \tag{18}$$

where $p_k = \dot{\epsilon}_{k-1}/\dot{\epsilon}_k$.

The boundary conditions (12) and (13) determine the initial values of the recursive relations (15) and (16) as

$$\alpha_0^l = 1,\ \beta_0^l = -1 \tag{19}$$

$$\alpha_N^u = 1,\ \beta_N^u = e^{2\gamma_{mn}t_N}. \tag{20}$$

Thus, with (15)–(20), all of the coefficients in (14) can be evaluated. The remaining work is to preserve the stability of the evaluation.

As mentioned in [10], there exists a numerical instability problem during the evaluation of (6) that arose from large values of γ_{mn}. When γ_{mn} grows, β_N and Γ_N rapidly converge to 1 and -1, respectively. In the meantime, $\tanh(\gamma_{mn}t_k)$ has an asymptote of 1, resulting in divided-by-zero, and $\cosh(\gamma_{mn}t_k)$ exceeds the maximum double precision very quickly.

In our evaluation of f_{mn}, the possible instability may lie in two aspects. The first is the recursive procedure (15) and (16), where the coefficients $a_k^{l,u}$ and $b_k^{l,u}$ are computed. When γ_{mn} increases, $e^{\gamma_{mn}t_k}$ may exceed the maximum double precision. We resolve this by defining a new data structure (actually, a C++ class) to handle super-large complex numbers, i.e., to express a general complex number z by

$$\mathbf{s\_cplx}\quad z = ae^x \begin{cases} a \in \text{complex} \\ x \in \text{double}. \end{cases}$$

The evaluation of (14)–(16) contains only five fundamental operations, i.e. "+," "−," "×," "/," and e^x (exponentiation). Moreover, the integration

$$\begin{aligned} \int f_{mn}(z,z')\mathrm{d}z = \frac{1}{\gamma_{mn}}&\left(\alpha_s e^{\gamma_{mn}z'}+\beta_s e^{-\gamma_{mn}z'}\right) \\ &\times(\alpha_f e^{\gamma_{mn}z}-\beta_f e^{-\gamma_{mn}z}) \end{aligned} \tag{21}$$

also contains these operations only. Thus, if the five operations are overloaded, the equations (14)–(16), as well as (21), can be computed using **s_cplx**. The overload is straightforward. As an example, the multiplication operator "×" is replaced by algorithm 1, where $z.a$ and $z.x$ are computed individually, and, if the norm of the resulting $z.a$ is larger than 10^5 or smaller than 10^{-5}, then it is *absorbed* by $z.x$. With all five operators being overloaded, the recursive evaluation of the coefficients in (14) can be performed stably.

Algorithm 1 Calculate $z = z_1 \times z_2$ for '**s_cplx**'

$z.a \Leftarrow z_1.a \times z_2.a$

$z.x \Leftarrow z_1.x + z_2.x$

if $|z.a| > 10^5$ or $|z.a| < 10^{-5}$ **then**

$z.x \Leftarrow z.x + \log(|z.a|)$

$z.a \Leftarrow z.a/|z.a|$

end if

Another potential instability may be caused by the denominator of (14). If $\alpha_s^u\beta_s^l$ and $\alpha_s^l\beta_s^u$ are both large and they are very close to each other, the denominator $(\alpha_s^u\beta_s^l - \alpha_s^l\beta_s^u)$ may become zero due to finite precision, resulting in a divided-by-zero. Fortunately, this problem is nonexistent. To examine this, the denominator can be written as $\alpha_s^u\alpha_s^l(r_s^l - r_s^u)$, where $r_s^l = \beta_s^l/\alpha_s^l$ and $r_s^u = \beta_s^u/\alpha_s^u$. Supposing γ_{mn} approaches ∞, it can be easily found from (15) and (16) that r_s^l has an asymptote of a constant $(1-p_s)/(1+p_s)$, while r_s^u approaches $(1+p_s)/(1-p_s)e^{2\gamma_{mn}t_k}$, i.e., they will not be close to each other.

The stability of the proposed approach can be testified by Fig. 2, where f_{mn} is plotted against $m(=n)$ for both lightly and heavily doped substrates described in Section VI-B. It can

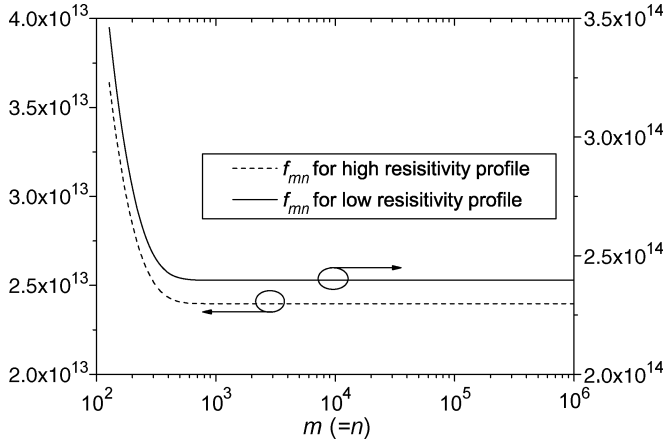

Fig. 2. f_{mn} as a function of $m(=n)$ in both low- and high-resistivity profiles.

be seen from the figure that, when m, n goes extremely large (up to a million), f_{mn} converges stably to a constant.

IV. Derivation of the Panel Integrations for 3-D Extraction

Suppose the coordinates of two conductors are as shown in Fig. 1. Each facet of the conductor is discretized to independent panels. To find $p_{ij} = \varphi_i/q_j$ with q_j assigned a unit value, (5) is integrated over the area of panel i and j. If one substitutes (5) into (2) and interchanges the order of the symbols, the integral can be computed analytically, resulting in a 2-D infinite summation.

To compute 3-D capacitance, the panels of a cuboid conductor can be grouped into three classes: horizontal (in the x–y) plane, vertical I (in the x–z plane), and vertical II (in the y–z plane). The positional combinations of each pair of panels can be classified into four types, as shown in Fig. 3. In type A, two panels are both bottom or top surfaces of the conductors. In type B, one panel is horizontal, and the other is vertical. In types C and D, both panels are vertical. They are parallel to each other in type C and perpendicular to each other in type D. In the following subsections, each type of panel pairs is discussed in turn.

A. Horizontal–Horizontal (Type A)

To compute the coefficient of two panels in the x–y plane, the Green's function is integrated over the panels. Excluding the cases of $m = 0$ and $n = 0$, the integration can be written as

$$p_{ij} = \sum_{m=1}^{S-1}\sum_{n=1}^{S-1} \frac{f_{mn}(z,z')}{s_1 s_2} \int_{a_1}^{a_2}\int_{b_1}^{b_2}\int_{a_3}^{a_4}\int_{b_3}^{b_4} \cos(\delta_m x')\cos(\xi_n y') \times \cos(\delta_m x)\cos(\xi_n y) dy dx dy' dx' \quad (22)$$

where S is the upper bound of the truncated infinite series. The integration in (22) can be evaluated analytically, resulting in sine functions, and it can be cast into a sum of 64 terms in the form

$$p_{ij} = \sum_{m=1}^{S-1}\sum_{n=1}^{S-1} \frac{f_{mn}}{s_1 s_2 \delta_m^2 \xi_n^2} \cos\left[\delta_m(a_{1,2} \pm a_{3,4})\right] \times \cos\left[\xi_n(b_{1,2} \pm b_{3,4})\right]. \quad (23)$$

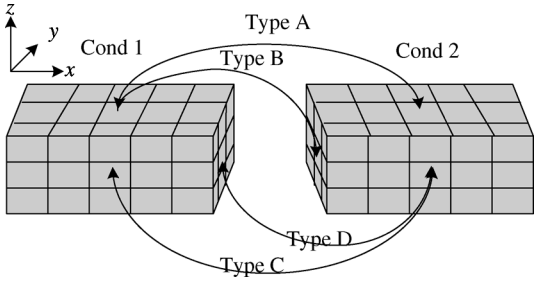

Fig. 3. Positional relations of two panels.

Thus, for a specific technology, the matrix of DCT, i.e.,

$$K_{pq} = \sum_{m=1}^{S-1}\sum_{n=1}^{S-1} \frac{f_{mn}}{\delta_m^2 \xi_n^2} \cos\left(m\pi\frac{p}{S}\right)\cos\left(n\pi\frac{q}{S}\right) \quad (24)$$

can be computed beforehand and stored in a database. When the layout information, i.e., the coordinates $a_1 - a_4$, and $b_1 - b_4$ and the areas s_1 and s_2 are given, the potential coefficients can be obtained by simply addressing in matrix $\mathbf{K}$ and summating the 64 terms.

B. Horizontal–Vertical (Type B)

For the case of type B, since a vertical panel is involved, the computation of potential coefficients consists of three integrations in the x- and y-directions and one integration in the z-direction. The integration of $f_{mn}(z', z)$ in the z-direction is shown as

$$f_{mn}^{(1)}(z') = \int_{c_1}^{c_2} f_{mn}(z', z) dz. \quad (25)$$

The closed-form solution of the above definite integration can be derived from (21).

The remaining three integrations in the x–y plane are the same as in type A. Supposing that the vertical panel is a field panel and it is in the x–z plane with the y-coordinate being b_f, the integration of potential coefficient can be written as

$$\begin{aligned} p_{ij} &= \sum_{m=1}^{S-1}\sum_{n=1}^{S-1} \frac{\cos(\xi_n b_f)}{s_1 s_2} \times \int_{a_1}^{a_2}\int_{b_1}^{b_2}\int_{a_3}^{a_4}\int_{c_3}^{c_4} \cos(\delta_m x')\cos(\xi_n y') \times \cos(\delta_m x) f_{mn}(z,z') dz' dx dy' dx' \\ &= \sum_{m=1}^{S-1}\sum_{n=1}^{S-1} \frac{f_{mn}^{(1)}}{s_1 s_2 \delta_m^2 \xi_n} \left[\sin(\xi_n b_2) - \sin(\xi_n b_1)\right] \times \cos(\xi_n b_f)\left[\sin(\delta_m a_2) - \sin(\delta_m a_1)\right] \times \left[\sin(\delta_m a_4) - \sin(\delta_m a_3)\right]. \end{aligned} \quad (26)$$

It can be cast into a sum of 32 terms similar to type A and turned into the form of a discrete cosine-sine transform

$$K_{pq} = \sum_{m=1}^{S-1}\sum_{n=1}^{S-1} \frac{f_{mn}^{(1)}}{\delta_m^2 \xi_n^2} \cos\left(m\pi \frac{p}{S}\right) \sin\left(n\pi \frac{q}{S}\right) \tag{27}$$

which is very similar to (24).

C. Vertical–Vertical (Types C and D)

For types C and D, the two panels are both vertical. The computation of p_{ij} consists of two integrations in the x–y plane and two integrations in the z-direction. Since the coefficients are discontinuous at the source point, depending on whether the two panels are in the same layer or not, the closed-form integration in the z-direction

$$f_{mn}^{(2)} = \int_{c_1}^{c_2}\int_{c_3}^{c_4} f_{mn}(z', z) dz dz' \tag{28}$$

should be derived individually. For both cases, the resulting expressions still consist of "+," "−," "×," "/," and e^x operations, such that the data structure **s_cplx** can also be used to preserve the computational stability.

The left derivation of p_{ij} includes two integrations in the x–y plane, and the resulting matrix $\mathbf{K}$ are DCT (for type C) and discrete sine transform (DST) (for type D), respectively. Due to space limitations, the details will not be presented here.

V. Efficient Green's Function Computation on Nonuniform Grid

In order to use FFT to compute (24), the chip should be discretized uniformly to $S \times S$ nodes, where S depends on $\max(a, b)$ and the minimum panel size Δ_m. Practically, to limit the discretization error, S should satisfy [15]

$$S \geq \frac{2\max(a, b)}{\Delta_m}. \tag{29}$$

With the shrinking metal width and larger chip size, S becomes larger and larger. In a typical circuit, $a = b = 1024$ μm and $\delta_m = 0.5$ μm, S will be at least 4096. If the technology has six metal layers and the sidewall capacitance is to be taken into account, about 150 Green's functions in total should be computed and saved. Even if FFT is used, the computational amount $\mathcal{O}(S^2 \log S^2)$ is still prohibitive. Moreover, to perform the FFT and store the results, the required memory size $\mathcal{O}(S^2)$ is unacceptable for most of today's PCs. In this section, a new technique is presented to reduce the computational time and memory. The following algorithm is presented for the case of type A defined in the previous section. The algorithm for other types can be derived similarly.

Let $x = p/S$ and $y = q/S$ be the normalized coordinates, thus $0 \leq x, y \leq 1$, and K_{pq} in (24) is a smooth function of x and y. $K(x, y)$ can be computed on some key nodes (x_i, y_j), $0 \leq i$, and $j < N_c$, where N_c is the amount of grid points

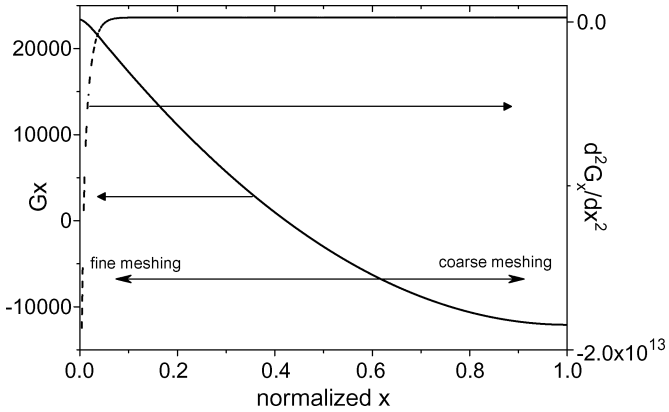

Fig. 4. $G_x(x)$ and $\partial^2 G_x/\partial x^2$, where $\partial^2 G_x/\partial x^2$ converges to a constant rapidly when x increases. x is normalized by $x' = x/a$.

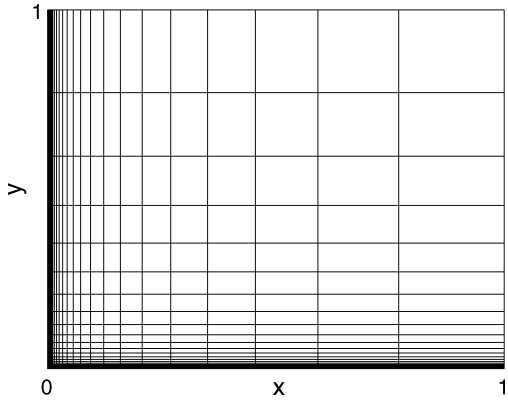

Fig. 5. Normalized nonuniform mesh grid for computing Green's function.

on both dimensions. The computed $K(x_i, y_i)$ is stored in the Green's function database, and interpolation can be involved when computing $K(x, y)$ for arbitrary (x, y).

It is easy to find that the potential coefficient p_{ij} is relevant to the second derivative of the transformed Green's function $K(x, y)$. $\partial^4 K/\partial x^2 \partial y^2$ approaches $-\infty$ when (x, y) approaches (0,0) and attenuates when x or y increases, as shown in Fig. 4. Thus, it is efficient to discretize the x–y plane with fine mesh when x and y are small, and with coarse mesh when they become large, i.e., to adopt nonuniform mesh grid. This is quite reasonable, since small x and y are related to near-field interaction and large x and y are related to far-field interaction, and the latter is obviously smoother and less important than the former.

An available meshing scheme is shown in Fig. 5, where x_i and y_i can be defined as

$$\begin{aligned} &x_0 = y_0 = 0, \\ &x_i = y_i = \frac{1}{\kappa^{N_c - 1 - i}}, \quad 1 \leq i \leq N_c - 1 \end{aligned} \tag{30}$$

where $\kappa > 1$ is a pregiven number. Thus, the minimum normalized mesh size (at $x = y = 0$) is $1/\kappa^{N_c - 2}$. For example, when $N_c = 35$, $\kappa = 1.5$, the minimum mesh size is $1/10^5$ of the chip size, which is sufficient for most cases. In case the minimum metal width Δ_m decreases or the maximum

lateral size $\max(a,b)$ increases, N_c can be set larger, proportioned to the logarithm of $\max(a,b)/\Delta_m$. As (29) holds, the storage requirement is therefor reduced from $\mathcal{O}(S^2)$ to $\mathcal{O}(N_c^2) = \mathcal{O}(\log^2(S_{\max}))$, where $S_{\max}$ is the potentially maximum value of S.

As a result of the nonuniform meshing, FFT is unavailable for acceleration. This may lead to $\mathcal{O}(S_{\max}^2 N_c^2)$ complexity if $K(x_i, y_i)$ is computed directly, which is slightly larger than that using DCT, which is $\mathcal{O}(S_{\max}^2 \log S_{\max}^2)$. However, by exploiting the property of f_{mn} in (14), the computation can be greatly accelerated. Let

$$r = \frac{a}{\pi}\gamma_{mn} = \sqrt{m^2 + (n\rho)^2} \tag{31}$$

where $\rho = a/b$ is the aspect ratio of the chip. Substituting r for (14), f_{mn} can be written as a function of r as

$$f_{mn}(z', z) = \left(\alpha_s e^{\frac{\pi z'}{a} r} + \beta_s e^{-\frac{\pi z'}{a} r}\right)\left(\alpha_f e^{\frac{\pi z}{a} r} + \beta_f e^{-\frac{\pi z}{a} r}\right). \tag{32}$$

Note that a_s, b_s, a_f, and b_f are all functions of r, thus $f(r)$ is a smooth function. Furthermore, $f(r)$ has an asymptote of a constant when r approaches infinity. Hence, $f(r)$ can be fitted by a certain function. In this paper, the following multipole-like expansion is used:

$$f(r) \approx \sum_{k=0}^{n_r} \frac{\chi_k}{r^k}, \quad r > M \cdot \sqrt{1+\rho^2} \tag{33}$$

where $M > 0$ is a pregiven number (such as 64) to avoid the computation of infinite $f(0)$ and preserve the precision of the approximation. n_r is the expansion order, for example $n_r = 4$, used to control the tradeoff between precision and computational complexity. When $m, n < M$, the sum of (35) is computed directly. When $m > M$ or $n > M$, the sum is computed by approximated $f(r)$.

Define matrix $\mathbf{T^k}$ with entries

$$T_{i,j}^k = \sum_{m \geq M \cup n \geq M}^{S-1} \frac{1}{m^2 n^2 r^k + 1} \cos(m\pi x_i)\cos(n\pi y_j). \tag{34}$$

Thus, each entry in matrix $\mathbf{K}$ in (24) can be partitioned into two parts as

$$\begin{aligned} K_{i,j} &= \sum_{m,n=1}^{S-1} \frac{a^2 b^2 f_{mn}}{m^2 n^2 \pi^4} \cos(m\pi x_i)\cos(n\pi y_j) \\ &\approx \frac{a^2 b^2}{\pi^4}\left[\sum_{m,n=1}^{M-1} \frac{f_{mn}}{m^2 n^2} \cos(m\pi x_i)\cos(n\pi y_j) \right. \\ &\qquad \left. + \sum_{k=0}^{n_r} \chi_k T_{i,j}^k\right] \end{aligned} \tag{35}$$

where the first portion consists of terms with indices m and $n < M$ and is computed directly, while the second portion includes the remaining and is computed approximately by (33) and (34).

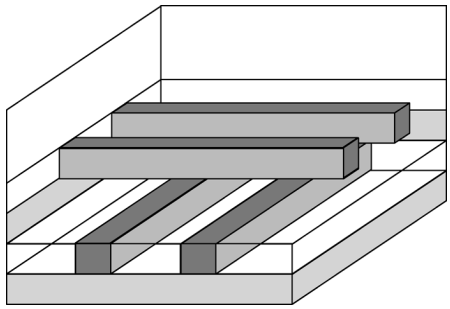

Fig. 6. 2×2 crossover in dielectrics.

The above procedure is summarized as follows.

1) Compute $\mathbf{T^k}$ using (34) for a series r and k. This is a purely maathematical problem and is independent of the technology and the layout.
2) Given a technology, compute $f(r)$ by (14) for a series of r.
3) Fit $f(r)$ to obtain coefficients χ_k by (33).
4) Compute matrix $\mathbf{K}$ by (35) and save it to the database.

As long as (34) has been computed, the fitting of $f(r)$ and the computation of (35) are fast and memory-efficient. For N_c^2 nodes, the computational time is approximately $\mathcal{O}(N_c^2 M^2)$, dominated by the first part in (35), and the memory for storing the matrix $\mathbf{K}$ is $\mathcal{O}(N_c^2)$.

Since FFT cannot be used for acceleration, the computation of (34) is very time consuming, and it may take several hours. Fortunately, (34) is layout- and technology-independent. Thus, it can be computed beforehand. Once computed, $\mathbf{T^k}$ can be stored and used for any technology and layout.

Once $K_{i,j}$, $0 \leq i, j \leq N_c$, is computed, for arbitrary coordinate pair (x, y), $K(x, y)$ can be computed by means of 2-D interpolation, such as spline interpolation [16].

VI. Numerical Results

The algorithm described above is implemented in the solver Substrate Coupling Analyzer for Passive Elements (SCAPE). Here, several examples will be shown to verify SCAPE and to compare the accuracy and efficiency with other methods. All simulations are done on a Sun Blade 2000 with Ultra SPARC III Cu processors at 900 MHz and 2-GB memory. Before the simulation of all of the following examples, the matrices $\mathbf{T^k}$ are computed for $N_c = 35$ and $S = 4096$, using about 1 h. Since $\mathbf{T^k}$ is technology-independent, it needs to be computed only once.

A. Test Cases for 3-D Extraction

The test cases are $k \times k$ $(k = 2, 3, 4, 5)$ crossing conductors in five dielectric layers, as shown in Fig. 6. Each conductor in the example is $(2k+1)$ (length) $\times 1 \times 1$ (cross section) (units in micrometers). The spacing between neighboring conductors in the same layer is 1 μm. The relative permittivity of every layer is 3.9. The thickness of the bottom four layers is 1 μm, and the thickness of the top layer is 28 μm. Each of the structures are surrounded by a $32 \times 32 \times 32$ box. The bottom of the box is a perfect ground plane, and the other five surfaces of the box are

TABLE I
COMPARISON FOR $k \times k$ BUS PROBLEMS

	Test problem			
	2×2	3×3	4×4	5×5
FastCap I (with fine mesh)				
CPU Time(s)	54	120	218	349
Memory (MB)	111	131	160	197
Panel #	7812	8724	9948	11492
FastCap II (with coarse mesh)				
CPU Time (s)	11.6	19.1	31.1	46.6
Memory (MB)	56	64	75	89
Panel #	3628	4080	4684	5448
Error (%)	2.89	2.84	2.85	2.76
ASITIC				
Panel #	50	84	144	220
Error (%)	23.7	24.8	25.8	25.4
SCAPE				
CPU time (s)	0.32	1.14	3.41	8.39
Memory (MB)	19	20	21	25
Panel #	146	276	464	700
Error (%)	0.99	0.91	1.60	2.38

in Neumann boundary condition, i.e., the normal derivative of the potential is zero.

The above crossover problems are computed by FastCap with very fine meshing (which is denoted by FastCap I), FastCap with relative coarse meshing (which is denoted by FastCap II), ASITIC, and SCAPE. The expansion order in both FastCap I and FastCap II is 2, which is the most accurate mode in running FastCap with a reasonable amount of time. In the input of FastCap, 0 is assigned to the permittivity of outer space to handle the boundary condition, and each interface between the dielectric layers is specified to make the comparison fair.

In ASITIC, since it cannot handle conductors with finite thickness, to model the thickness effect to the best of its abilities, the upper and lower surfaces of the conductors are treated independently as conductors of zero thickness and are extracted as such. After extraction, the resulting matrix is reduced by combining together the top and the bottom plates of the conductors. This is electrically equivalent to shorting the top and the bottom plates together [13].

Using the capacitance matrix $\mathbf{C}$ of FastCap I, i.e., FastCap with very fine meshing, as the standard, the error of capacitance matrix $\mathbf{C}'$ computed by another program is estimated in a two-norm manner: $||\mathbf{C}'-\mathbf{C}||/||\mathbf{C}||$. The error of FastCap II is around 3%, which is controlled by adjusting the mesh size.

Table I compares SCAPE with ASITIC and FastCap. It is shown that, using FastCap I's result as the criterion, SCAPE is more accurate than FastCap II, which is within 2.5% and around 3%, respectively. ASITIC does not account for the sidewall effect, and thus it results in large error ($> 20\%$).

B. Test Cases for Nonuniform Grid Method

This example shows the advantage of using the efficient computation of Green's function as presented in Section V. Two experiments using different substrate profiles are conducted to test the accuracy and efficiency of the extraction algorithm. The profiles used are taken from [17] and described in Fig. 7. The high-resistivity substrate is used in various BiCMOS processes, while the low-resistivity substrate is used in CMOS due to the

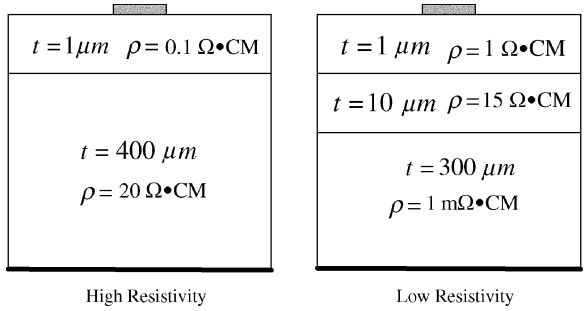

Fig. 7. Substrate profiles used in example problem.

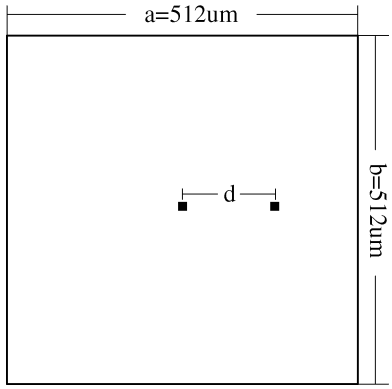

Fig. 8. Two contacts over the top of the substrate. This case is used to verify the nonuniform grid method and compare the accuracy and efficiency with the DCT method.

TABLE II
SUMMARY OF COMPARISON. ERROR IS WITH RESPECT TO DCT-1024

method	FFT-size	Avg. Err.	Mem (MB)	Time (s)
DCT	2048	–	67	49.6
DCT	1024	–	17	12.6
DCT	512	6.35%	4.2	3.1
DCT	256	43%	1.0	0.76
SCAPE	–	0.94%	0.18	0.2

latch-up suppressing properties. The test example is shown in Fig. 8, where two conductors lie over a substrate with an oxide layer. To simplify the comparison, the thickness of the conductors is set to zero, and thus the sidewall effect is ignored. The distance between the centers of two conductors is d μm. The substrate laterals for both profiles are $a = b = 512$ μm.

The Green's functions for both profiles were computed and compared in Table II, from which it is seen that: 1) SCAPE is much more accurate than DCT-512 (i.e., the DCT method with the FFT size of 512); 2) in the stage for computing the Green's function, SCAPE is about 16× faster than DCT-512 and uses 1/24 of the memory used by DCT-512. Compared with DCT-1024, SCAPE is about 64× faster and uses only 1/95 of the memory. If the contact size decreases, the required FFT size and the time and memory usage for the DCT method will be increase quadratically, while, for the nonuniform grid method, the required time and memory usage stay constant for a wide range of contact sizes. Figs. 9 and 10 show the extrapolated time and memory used for the DCT method and nonuniform grid method. In the DCT method, the required memory and time

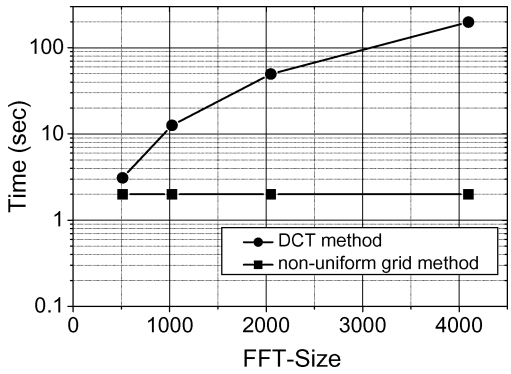

Fig. 9. Computational cost of Green's function as a function of the required FFT size. The circle symbol line shows the variation of the DCT based method, while the square symbol line shows the nonuniform grid method.

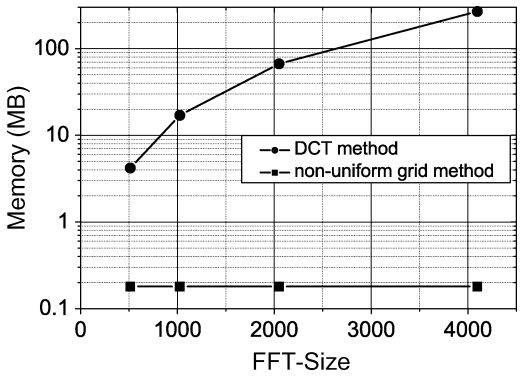

Fig. 10. Memory required for storing the Green's function as a function of the required FFT size. The circle symbol line shows the variation of the DCT-based method, while the square symbol line shows the nonuniform grid method.

usage for DCT-4096 are 269 MB and 198 s, respectively. It is noticeable that, for a six-layer technology, considering the sidewall effect and ten frequency points, a factor of 1500 would be multiplied on them, and the cost is unacceptable.

Three classes of test were done to verify the accuracy of the nonuniform grid method. In the first test, the two contacts are both of size 2 μm, and the distance between them is 100 μm, the frequency varies from 1 to 20 GHz. In the second test, the size and the frequency are fixed at 2 μm and 1 GHz, and the distance varies from 2 to 100 μm. In the third test, the distance and the frequency are fixed at 100 μm and 1 GHz, and the size of both contacts varies from 8 to 0.25 μm. The results are compared in Table III, where the impedance obtained by the nonuniform grid method and DCT method is comparable.

We applied the proposed method to a relatively large-scale circuit with the layout from a simple mixed-signal circuit. Fig. 11 shows the layout for an example problem with 67 contacts on a 512 μm $\times$ 512 μm substrate. For each of the substrate profiles shown in Fig. 7, extraction was performed, and the resulted capacitance matrix is converted into an impedance matrix. The comparison of impedance computed by the DCT method and the nonuniform grid method is shown in Table IV. It is seen from the table that the results from both of the methods are comparable.

TABLE III
COMPARISON OF EXTRACTED IMPEDANCE AS A FUNCTION OF FREQUENCY USING HIGH-RESISTIVITY PROFILE

	DCT (FFT-size=1024)		Nonuniform Grid	
	High Prof.	Low Prof.	High Prof.	Low Prof.
Freq (GHz) (distance = 100 μm, size = 2 μm)				
1	3690	2485236	3704	2527208
2	3718	2479728	3732	2521608
5	3904	2442155	3920	2483406
10	4450	2320462	4468	2359671
15	5125	2152146	5147	2188528
20	5832	1967527	5858	2000804
Distance (μm) (frequency = 1 GHz, size = 2 μm)				
2	561	43233	567	44241
4	878	95547	884	97473
10	1394	245056	1400	250918
20	1897	494496	1905	503145
30	2253	746153	2262	756568
50	2786	1253865	2795	1272968
Size (μm) (frequency = 1 GHz, distance = 100 μm)				
0.25	68391	170037106	117469	153040652
0.50	9204	30136738	11957	39878202
1.00	5616	9554460	5720	10088130
2.00	3690	2485236	3704	2527208
4.00	2653	627658	2654	630433
8.00	1946	156906	1945	157035

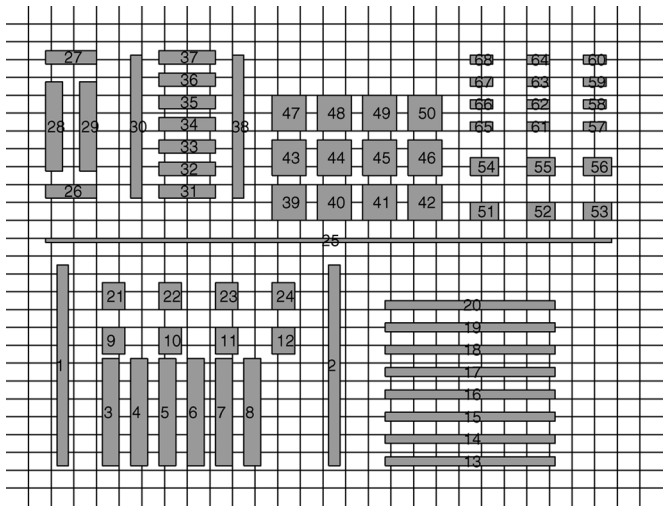

Fig. 11. Example layout from a mixed-signal design.

TABLE IV
SELECTED SET OF EXTRACTED IMPEDANCE FOR THE EXAMPLE LAYOUT

$\|Z_{ij}\|$		Method in [10]		SCAPE	
i	j	High Resis.	Low Resis.	High Resis.	Low Resis.
1	1	3591	267	3589	268
1	10	41962	5536144	42707	7445965
2	2	6281	269	6278	269
2	18	1684	41995	1679	41705
5	15	370584	41490698	350322	41699653
10	10	60371	1463	60446	1465
20	49	381088	39427248	409429	39852996
30	50	319259	38782910	373999	38726794
40	64	1728364	176068325	1763526	176612558

C. Interdigital Capacitor (IDC) Over Lossy Substrate

The major advantage of SCAPE over capacitance extraction programs based on free-space Green's function, such as

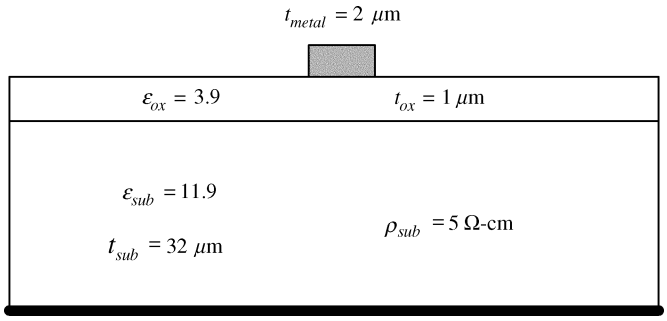

Fig. 12. Substrate structure for the IDC.

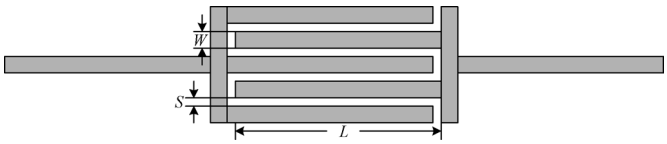

Fig. 13. Structure of the IDC.

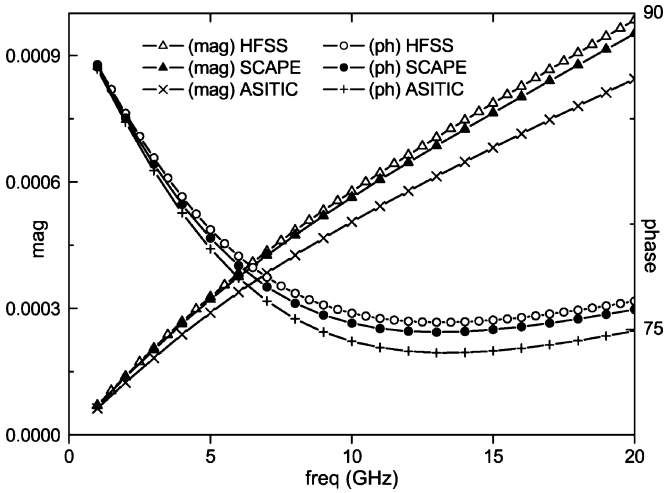

Fig. 14. Y_{11} of the IDC.

FastCap, is its capability of dealing with multilayered dielectric and conductive substrate. This capability provides complex capacitance and its frequency dependency. The example is the simulation of an IDC (or fractal capacitor), and it demonstrates the frequency-dependent capacitance extraction.

The hypothetical process used in this example is shown in Fig. 12. We choose HFSS [2] for comparison. HFSS is a widely used commercial software based on the finite-element method (FEM), and it supports full-wave simulation. In order to obtain a reasonable accuracy in HFSS within acceptable memory and time, the thickness of the substrate is set to be 32 μm.

As shown in Fig. 13, the structure of the IDC is defined by the finger length L, finger width W, spacing S, and the number of fingers N_f. The parameters of the simulated IDC are $L = 15$ μm, $W = 2$ μm, $S = 2$ μm, and $N_f = 5$.

Figs. 14 and 15 show the Y_{11}- and Y_{21}-parameters, respectively, computed by HFSS, ASITIC, and SCAPE. The results from HFSS are taken as the reference, where the magnitude and

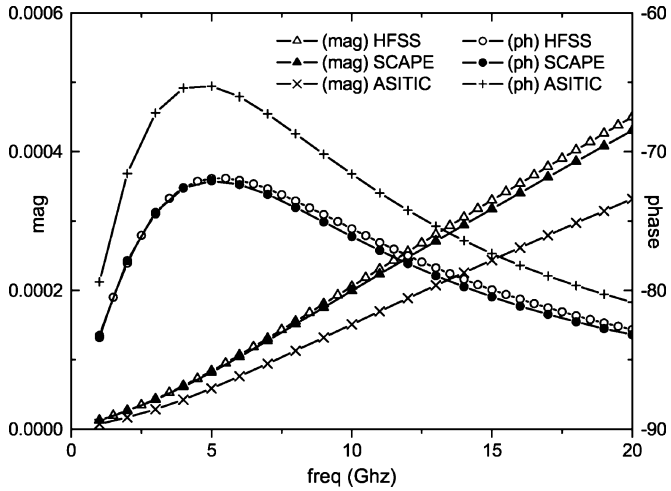

Fig. 15. Y_{21} of the IDC.

phase of Y-parameters are sensitive to frequency due to the substrate loss. Both the ASITIC and SCAPE curves show the right trend when the frequency increases. However, since ASITIC does not compute the sidewall capacitance, the discrepancy between ASITIC and HFSS is unacceptably large, while the average error between SCAPE and HFSS is less than 3%. Since HFSS supports full-wave simulation while SCAPE is a quasi-static method, this example also indicates that the quasi-static assumption is still applicable up to 20 GHz without noticeable error.

VII. Conclusion

An improved Green's function-based algorithm is proposed for the extraction of 3-D capacitance on the lossy substrate at RF frequency. A new formula is adopted, and the Green's function can be integrated analytically and stably in the z-direction, thus the capacitance of the sidewall surfaces can be evaluated. In addition, to reduce the computational time and memory requirement in computing, transforming, and storing the Green's function, a novel nonuniform grid method is developed and proposed. The memory requirement and the computational complexity reduce from $\mathcal{O}(S^2)$ and $\mathcal{O}(S^2 \log S^2)$, respectively, to $\mathcal{O}[(\log S_{\max})^2]$ for both.

Acknowledgment

The authors would like to thank the staff of Cadence, San Jose, CA, for their collaboration.

References

[1] *"Raphael User's Manual,"* Synopsys, Mountain View, CA, 2004.
[2] *"Ansoft HFSS User's Manual,"* Ansoft Corporation, Pittsburgh, PA, 2001.
[3] K. Nabors and J. White, "FastCap: a multipole accelerated 3-d capacitance extraction program," *IEEE Trans. Computer-Aided Design Integr. Circuits Syst.*, vol. 10, no. 11, pp. 1447–1459, Nov. 1991.
[4] S. Kapur and D. E. Long, "IES3: a fast integral equation solver for efficient 3-dimensional extraction," in *Proc. Int. Conf. Computer Aided Design*, San Jose, CA, Nov. 1997, pp. 448–455.

[5] W. Shi, J. Liu, N. Kakani, and T. Yu, "A fast hierarchical algorithm for three-dimensional capacitance extraction," *IEEE Trans. Comput.-Aided Design Integr. Circuits Syst.*, vol. 21, no. 3, pp. 330–336, Mar. 2002.
[6] W. Yu and Z. Wang, "Enhanced QMM-BEM solver for three-dimensional multiple-dielectric capacitance extraction within the finite domain," *IEEE Trans. Microw. Theory Tech.*, vol. 52, no. 2, pp. 560–566, Feb. 2004.
[7] C. H. Chan and L. Tsang, "A sparse-matrix canonical-grid method for scattering by many scatterers," *Microw. Opt. Technol. Lett.*, vol. 8, no. 2, pp. 114–118, 1995.
[8] M. B. E. Bleszynski and T. Jaroszewicz, "AIM: adaptive integral method for solving large-scale electromagnetic scattering and radiation problems," *Radio Sci.*, vol. 31, no. 5, pp. 1225–1251, 1996.
[9] R. Gharpurey and R. G. Meyer, "Modeling and analysis of substrate coupling in integrated circuits," *IEEE J. Solid-State Circuits*, vol. 31, no. 3, pp. 344–353, Mar. 1996.
[10] A. M. Niknejad, R. Gharpurey, and R. G. Meyer, "Numerically stable Green function for modeling and analysis of substrate coupling in integrated circuits," *IEEE Trans. Comput.-Aided Design Integr. Circuits Syst.*, vol. 17, no. 4, pp. 305–315, Apr. 1998.
[11] S. Ramo, J. R. Whinnery, and T. V. Duzer, *Fields and Waves in Communication Electronics*, 3rd ed. New York: Wiley, 1994.
[12] A. M. Niknejad and R. G. Meyer, "Analysis, design, and optimization of spiral inductors and transformers for Si RF IC's," *IEEE J. Solid-State Circuits*, vol. 33, no. 10, pp. 1470–1481, Oct. 1998.
[13] R. Gharpurey and S. Hosur, "Transform domain techniques for efficient extraction of substrate," in *Proc. Int. Conf. Computer Aided Design*, San Jose, CA, 1997, pp. 461–467.
[14] R. Gharpurey, "Modeling and analysis of substrate coupling in integrated circuits," Ph.D. dissertation, College of Eng., Univ. of California, Berkeley, 1999.
[15] C. Xu, T. Fiez, and K. Mayaram, "On the numerical stability of Green's function for substrate coupling in integrated circuits," *IEEE Trans. Comput.-Aided Design Integr. Circuits Syst.*, vol. 24, no. 4, pp. 653–658, Apr. 2005.
[16] C. de Boor, *A Practical Guide to Splines*. New York: Springer-Verlag, 1978.
[17] J. P. Costa, M. Chou, and L. M. Silveira, "Efficient techniques for accurate modeling and simulation of substrate coupling in mixed-signal ICs," *IEEE Trans. Comput.-Aided Design Integr. Circuits Syst.*, vol. 18, no. 5, pp. 597–607, May 1999.

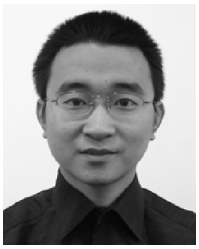

Zuochang Ye (S'05) was born in Hainan, China, on October 17, 1979. He received the B.S. degree in electronics engineering from Tsinghua University, Beijing, China, in 2002, and is currently working toward the Ph.D. degree in microelectronics at Tsinghua University.

His interests are in the area of RF circuit modeling, substrate coupling, and numerical methods in electromagnetics.

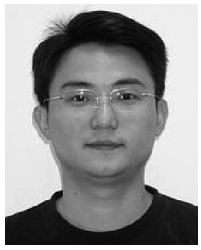

Wenjian Yu (S'01–M'04) received the B.S. and Ph.D. degrees in computer science (both with the highest honors) from Tsinghua University, Bejing, China, in 1999 and 2003, respectively.

Since August 2003, he has been a Research Assistant in the Department of Computer Science and Technology, Tsinghua University. His research interests include the parasitic parameter extraction of interconnects in very large-scale integration (VLSI) circuits, the direct boundary element analysis of the electromagnetic field, and the modeling and simulation of VLSI interconnects. He published more than 40 technical papers in refereed journals or conferences.

Dr. Yu was the Technical Program subcommittee member of the ACM/IEEE Asia South-Pacific Design Automation Conference in 2005. He was the recipient of the Microsoft Fellowship Award in 2002 and the distinguished Ph.D. Award from Tsinghua University in 2003. He has served as a reviewer for the IEEE TRANSACTIONS ON COMPUTER-AIDED DESIGN OF INTEGRATED CIRCUITS AND SYSTEMS and the IEEE TRANSACTIONS ON MICROWAVE THEORY AND TECHNIQUES.

Zhiping Yu (S'80–M'80–SM'94) received the B.S. degree from Tsinghua University, Beijing, China, in 1967, and the M.S. and Ph.D. degrees from Stanford University, Stanford, CA, in 1980 and 1985, respectively.

He is presently a Professor and Deputy Director with the Institute of Microelectronics, Tsinghua University. From 1989 to 2002, he was a Senior Research Scientist with the Department of Electrical Engineering, Stanford University, while serving as a faculty member with Tsinghua University. He returned to Tsinghua University full time in September 2002 and held the Pericom Microelectronics Professorship (2002–2004). His research interests include device simulation for nanoscale MOSFETs, quantum transport in nanoelectronic devices, compact circuit modeling of passive and active components in RF CMOS, and numerical analysis techniques. He has authored or coauthored over 170 technical papers and coauthored the book on technology for computer-aided design *Technology CAD—Computer Simulation of IC Processes and Devices* (Kluwer, 1993). He served as the Associate Editor of the IEEE TRANSACTIONS ON COMPUTER-AIDED DESIGN OF INTEGRATION OF CIRCUITS AND SYSTEMS from 1996 to 2005.